Low accretion rates in black holes in late-stage merger ultraluminous infrared galaxies

Rieke, G.H.; Buiten, V.A.; Goldberg, C.E.; Morrison, J.; Werf, P.P. van der; Alonso-Herrero, A.; ... ; Zhu, Y.

The Astrophysical Journal, 988:17 (11pp), 2025 July 20 https://doi.org/10.3847/1538-4357/add2fd

Low Accretion Rates in Black Holes in Late-stage Merger Ultraluminous Infrared Galaxies

George H. Rieke[1], Victorine A. Buiten[2], Charles E. Goldberg[3], Jane Morrison[1], Paul van der Werf[2], Almudena Alonso-Herrero[4], Stacey Alberts[1], Nina Bonaventura[1], Zhiyuan Ji[1], Jianwei Lyu[1], P. Rinaldi[1], Meredith A. Stone[1], Yang Sun[1], and Yongda Zhu[1]
[1] Steward Observatory, University of Arizona, 933 North Cherry Avenue, Tucson, AZ 85721, USA
[2] Leiden Observatory, Leiden University, PO Box 9513, 2300 RA Leiden, The Netherlands
[3] Department of Astronomy and Astrophysics, University of California, San Diego, 9500 Gilman Drive, La Jolla, CA 92093, USA
[4] Centro de Astrobiología (CAB), CSIC-INTA, Camino Bajo del Castillo s/n, E-28692 Villanueva de la Cañada, Madrid, Spain
Received 2025 January 14; revised 2025 April 7; accepted 2025 April 29; published 2025 July 10

Abstract

We explore the accretion rates of supermassive black holes (SMBHs) in late-stage galaxy mergers by observing three ultraluminous infrared galaxies (ULIRGs), IRAS 14378-3651, IRAS 17208-0014 and IRAS 23365+3604, using the JWST/MIRI Medium Resolution Spectrometer and JWST/NIRSpec integral field unit. In all three cases, we fail to detect [Ne VI] λ7.65 μm, a robust active galactic nuclei (AGN) tracer lying in a low-opacity interstellar window, nor do we detect any other lines that might indicate AGNs. The only detected high-excitation emission line, [Mg IV] (λ4.488 μm), arises from shocks associated with supernovae. Our new, deep flux limits on AGN tracers in the near- and mid-infrared indicate that the nuclear obscuration of any purported AGNs in our sample is isotropic, i.e., the far-infrared luminosities of these galaxies are unlikely to be driven by escaping AGN power. This allows us to show that the Eddington ratios of their SMBHs are low. We then assemble an unbiased sample of 19 ULIRGs (from the IRAS Bright Galaxy Sample with $L(\mathrm{TIR}) \geqslant 10^{12}\,L_{\odot}$) in late-stage mergers and show that their dynamically measured black hole masses are consistent with the values from scaling from their stellar masses. On this basis, we show that the Eddington ratios of any AGNs in 15 of these galaxies are also very low, $\lesssim$10%. This indicates that any black holes are in a relatively quiescent state. That is, high levels of accretion are found in only a minority of late-merger-phase ULIRGs.

Unified Astronomy Thesaurus concepts: Ultraluminous infrared galaxies (1735)

1. Introduction

The hypothesis that quasars are born in merging ultraluminous infrared galaxies (ULIRGs; D. B. Sanders et al. 1988) is central to our understanding of the evolution of active galactic nuclei (AGNs). This paradigm has prompted multiple theoretical studies of how, in detail, the AGN birth process may proceed (P. F. Hopkins et al. 2008; G. F. Snyder et al. 2013; J. M. Gabor et al. 2016; C. Ricci et al. 2017; T. Kawaguchi et al. 2020; J. McKinney et al. 2021). The first stages of AGN ignition are expected to be hidden deep within opaque dust clouds, but as the galaxy merger progresses the dust is cleared by outflowing winds and the AGN is revealed. A central theme is that ULIRGs in the late stages of mergers must be ideal systems for (a) allowing high rates of accretion onto the black hole(s) of these merging galaxies, and (b) disrupting and clearing dusty materials to reveal the AGN as a quasar. The theoretical connection among galaxy mergers, ULIRGs, and AGNs was reinforced by the discovery of AGNs associated with many local ULIRGs (e.g., D. B. Sanders & I. F. Mirabel 1996).

There seem to be no real theoretical alternatives to the general idea that ULIRGs or similar galaxies (e.g., somewhat lower-luminosity starbursts) are the birthplaces of quasars. However, the details are complex. For example, among the late-stage merger ULIRGs ($\log(L_{\mathrm{IR}}) > 12$) from S. Stierwalt et al. (2013), only slightly more than half have relatively luminous AGNs (based on classifications in the NASA Extragalactic Database, NED). While most of the remainder seem to be uncomplicatedly dominated by star formation, there is a stubborn subset, exemplified by Arp 220, with extreme nuclear properties including very dense gas but only weak or inconclusive evidence of an AGN. The most extreme of these cases have been dubbed compact obscured nuclei (CONs; see, e.g., N. Falstad et al. 2021). CONs are thought to be embedded so deeply that their interior energy is nearly completely thermalized and emitted in the infrared. This obscuration obliterates most clues to the nature of the underlying emitting source, and might be considered an insurmountable obstacle to their study. However, if the obscuration is complete, we can determine the bolometric luminosity (or its upper limit) and use it to constrain the properties of any embedded AGN.

In this paper, we investigate the ULIRGs IRAS 14378-3651, IRAS 17208-0014 (also known as IRAS F17207-0014), and IRAS 23365+3604, along with Arp 220, which we examined in detail in a previous study (C. E. Goldberg et al. 2024). All four galaxies are late-stage mergers (S. Haan et al. 2011; S. Stierwalt et al. 2013) and have compact nuclear sources with very strong obscuration (S. Stierwalt et al. 2014). The latter three are dense enough to be classified as CONs. No galaxy in this sample has decisive evidence of an embedded AGN, despite substantial, multiwavelength detection efforts. The result is that the literature is full of contradictory claims about the presence or absence of AGN activity in these galaxies. We utilize the unprecedented sensitivity of JWST's NIRSpec and MIRI instruments to search for evidence of

AGNs, and discuss the nature of the embedded nuclear sources.

We then expand the study to a complete sample of 19 late-stage ULIRGs. Although some of this sample have luminous AGNs, the majority have no strong evidence for AGNs and, indeed, we find that any AGNs must have low Eddington ratios, <10%. The Eddington ratio for the sample as a whole is also small, ∼0.03. This result shows that the high levels of accretion predicted for such cases by many theoretical models are likely to occur for only a fraction of the galaxies.

In Section 2, we introduce each galaxy in our sample and summarize their existing data. Our NIRSpec and MIRI observations, data reduction process, and analysis are described in Section 3. We present the results of our spectral analysis in Section 4. We discuss the implications for the properties of any AGNs in these galaxies and in an expanded sample of 19 ULIRGs in Section 5. Section 6 derives Eddington ratios for the entire sample, and we summarize the results from the paper in Section 7. An Appendix discusses the properties of the high-excitation [Mg IV] line detected in the spectra of all three galaxies.

2. Description of the Galaxies

We have obtained deep JWST spectra of the four ULIRGs described below to improve our understanding of their properties regarding possible nuclear AGNs. We will use this understanding to expand our discussion to a complete sample of 19 in Section 5.

Arp 220. The relevant properties of Arp 220 are summarized in an accompanying paper (C. E. Goldberg et al. 2024) and in M. Perna et al. (2024). It is the closest ULIRG, at a distance of ∼83 Mpc, and can be observed at excellent physical resolution. It has two nuclei separated by only 1″, or ∼400 pc, showing it is in a late merging stage; the galaxy outside of the nucleus has post-starburst properties as theoretically expected for such a merger (R. Chandar et al. 2023). Atacama Large Millimeter/submillimeter Array observations by N. Falstad et al. (2021) measured the strength of $\Sigma_{\rm HCN\text{-}vib} = 11.96 \pm 2.31\, L_\odot\, {\rm pc}^{-2}$ for the west nucleus, showing that it is an extreme CON and the east nucleus with $\Sigma_{\rm HCN\text{-}vib} = 0.95 \pm 0.22\, L_\odot\, {\rm pc}^{-2}$ is a near-CON (where a value >1 would identify a CON; N. Falstad et al. 2021). In the mid-infrared, extremely deep silicate absorption ($\tau = 6.10 \pm 0.03$) also indicates extremely high nuclear obscuration (e.g., S. Stierwalt et al. 2014). C. E. Goldberg et al. (2024) failed to find any indications of an AGN, e.g., [Ne v] or [Ne VI], in mid-infrared spectroscopy from JWST/MIRI.

In the very hard X-ray with NuSTAR, S. H. Teng et al. (2015) found no evidence for an AGN despite the deep observation above 10 keV. C. E. Goldberg et al. (2024) used deep Fe-Kα reflected-line measurements to deduce intrinsic 2–10 keV luminosities for the two nuclei, to which they applied a bolometric correction of a factor of 13.7 (F. Duras et al. 2020; C. Auge et al. 2023). This indicates a total AGN luminosity of $4 \times 10^{10}\, L_\odot$, about 2.5% of the total infrared luminosity.

IRAS F14378-3651. This galaxy is classified as a "Sy2: ULIRG LINER" in NED and as a Sy2 in P.-A. Duc et al. (1997) and I. Lamperti et al. (2022). There is an upper limit on the vibrationally excited HCN that indicates this nucleus is well below CON level ($\Sigma_{\rm HCN-vib} \leqslant 0.025\, L_\odot\, {\rm pc}^{-2}$ for both nuclei). In agreement with this trend, the depth of the 9.7 μm silicate absorption is $\tau = 2.95 \pm 0.03$, also much less than for Arp 220. The equivalent widths (EWs) of the polycyclic aromatic hydrocarbon (PAH) features also put this out of the CON range (F. R. Donnan et al. 2023). Therefore, we expect that traces of any AGN would possibly escape from the obscured nuclei. S. H. Teng et al. (2015) find an intrinsic 2–10 keV X-ray luminosity of $\sim 3 \times 10^8\, L_\odot$, corresponding (after applying the factor of 13.7 correction) to a bolometric AGN luminosity ∼0.3% of the total infrared luminosity.

IRAS 17208-0014. This galaxy is very well studied. S. Arribas & L. Colina (2003) find that the true nucleus is displaced from the apparent optical one and that the spectral type is that of a low-ionization nuclear emission-line region (LINER). Based on HCN measurements, this galaxy is a CON ($\Sigma_{\rm HCN\text{-}vib} = 2.15 \pm 0.38\, L_\odot\, {\rm pc}^{-2}$), although not so extreme as the dominant nucleus in Arp 220 (Arp 220 W). The silicate feature depth is $\tau = 4.58 \pm 0.04$ (S. Stierwalt et al. 2014), trending similarly to the HCN-vib results. The EWs of the PAH features support the classification of this as a CON (F. R. Donnan et al. 2023). There is no detectable hard X-ray flux with NuSTAR (C. Ricci et al. 2021). However, based on Chandra and XMM-Newton results, O. González-Martín et al. (2009) identify a Compton-thick (CT) AGN in the galaxy with an obscuration-corrected 2–10 keV luminosity of $\log L_X = 42.97$. Applying a bolometric correction, the total AGN luminosity would be $3.4 \times 10^{10}\, L_\odot$, about 2% of the total infrared luminosity.

As with Arp 220, IRAS 14378-3651, and IRAS 23365 +3604, there are strong outflows (e.g., D. S. N. Rupke & S. Veilleux 2013; S. Arribas et al. 2014; S. García-Burillo et al. 2015); in addition, the gas velocity structure of this galaxy is very complex (A. M. Medling et al. 2015; S. Baba et al. 2022). The luminosity of any AGN derived from X-rays (above) and in our discussion in Section 5.2 is inadequate to power the outflows (S. García-Burillo et al. 2015). As the authors point out, an even more deeply obscured AGN might be able to power them, but this would be surprising given the very low Eddington ratio (∼0.007) we derive for this galaxy's nucleus. However, the outflows may be fossils, indicating much higher luminosity in the past (e.g., K. Zubovas et al. 2022). Alternatively, they may be powered by the extreme density of star formation (e.g., A. Gowardhan et al. 2018).

IRAS 23365+3604. The silicate feature depth is $\tau = 3.59 \pm 0.03$ (S. Stierwalt et al. 2014); by comparison with the values of the other CONs in N. Falstad et al. (2021), this makes it quite possibly a CON. The PAH EW ratio method described by F. R. Donnan et al. (2023) shows one ratio in the CON range and the other out of it, consistent with this being at least a near-CON. There is no detectable hard X-ray flux with NuSTAR (C. Ricci et al. 2021). From Chandra measurements, K. Iwasawa et al. (2009) find a 2–10 keV luminosity of $\log L_X = 41.20$. This would indicate a ratio of X-ray to infrared luminosities <<1%, although an accurate estimate is not possible because the X-ray luminosity is not corrected for obscuration.

For all four of these galaxies, [Ne v] is not detected with Spitzer (H. Inami et al. 2013).

3. Data

Data for IRAS F14378-3651, IRAS 17208-0014, and IRAS 23365+3604 were collected with the JWST MIRI Medium Resolution Spectrometer (MRS) and NIRSpec integral field unit (IFU) as part of Cycle 1 GTO program 1204 (PI: George Rieke; DOI: 10.17909/b09a-6782). For MIRI data, the most diagnostic high-excitation line is [Ne VI] 7.652 μm, as discussed in C. E. Goldberg et al. (2024). We therefore obtained

Table 1
NIRSpec Observation Parameters

Grating/Filter	Wavelength Range (μm)	Integration Time (s)
G140H/F100LP	0.97–1.89	583
G235H/F170LP	1.66–3.17	583
G395H/F290LP	2.87–5.27	525

Note. The field of view and resolving power for all observations are $3'' \times 3''$ and 2700, respectively.

measurements only in subband A of each of the four main channels, otherwise the procedures were similar to those described by C. E. Goldberg et al. (2024). Twelve exposures were taken for each galaxy, with a dither every third frame; 28 minutes of exposure time were used for each MRS detector, resulting in a total exposure time of 56 minutes of MIRI data for each galaxy. The MIRI data were reduced in the JWST pipeline (version 1.13.4), with the reference files from CRDS context jwst_1197.pmap. The background was subtracted in an image-to-image subtraction process. We utilized the built-in pipeline tool to flag MIRI cosmic-ray "shower" events and applied residual fringe correction in the `calwebb_spec` pipeline. An additional tool using the background images was used to flag additional bad pixels.[5] The final data product is a cube for each channel. Each cube is approximately 30×40 pixels, and the spectral resolution varies depending on wavelength.

For NIRSpec, diagnostic lines are spread over the full spectral range. If lines escape from the central region by scattering, then shorter-wavelength lines may be favored. Therefore, the data were acquired using the high-resolution ($R \approx 2700$) gratings, with three grating/filter configurations used (Table 1). For each galaxy, four exposures were taken through each configuration for a total of 28 minutes on each galaxy, with a dither being executed after every exposure. The NIRSpec data were reduced in the JWST pipeline (version 1.14.1), with the reference files from CRDS context jwst_1223.pmap. We utilized the built-in pipeline tool to flag NIRSpec cosmic-ray "snowball" events and applied a $1/f$ noise correction (NSClean) in the `calwebb_spec` pipeline. NIRSpec data suffer from outlier pixels that can cause spikes and noise in the extracted spectrum. No satisfactory algorithm has been developed to flag these pixels. Instead, we studied the data quality of the pixels and found a set of flags that we set as a bad-pixel indicator.[6] In addition, when building the final data product an optional step of flagging outliers using the "outlier_detection" step in `calwebb_spec3` was used.

For both MIRI and NIRSpec, the data were converted to three-dimensional data cubes, with the x-, y-, and z-coordinates corresponding to R.A., decl., and wavelength.

After the spectra were reduced, bright emission lines were measured and identified. Then, they were fitted using least squares to measure the redshift of each galaxy. Redshifts of 0.068154, 0.042664, and 0.064172 were found for IRAS 14378-3651, IRAS 17208-0014, and IRAS 23365+3604, respectively. These values agree well with standard redshifts from NED of 0.0676, 0.0428, 0.0645.

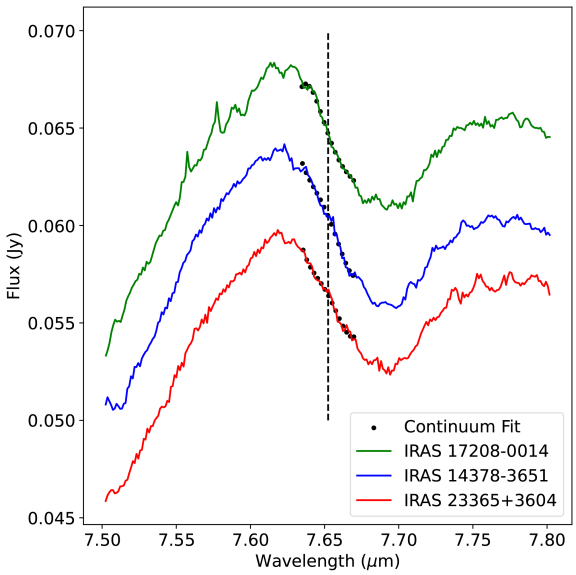

Figure 1. Extraction of the [Ne VI] line. The flux scale is for IRAS 14378-3651, which is the middle spectrum (blue). The spectra for the other two galaxies have been arbitrarily shifted for display, with IRAS 17208-0014 at the top (green) and IRAS 23365+3604 at the bottom (red). The spectra are dominated by methane ice, although other molecular features due to acetylene can be seen in the shorter-wavelength part of the spectrum of IRAS 17208-0014. The models used to fit the absorptions are shown around the wavelength of the [Ne VI] line ("continuum fit") for comparison with the spectra. The wavelength of the [Ne VI] line is shown with the vertical dashed line.

In extracting the high-excitation spectral lines we needed to adopt an aperture diameter and line width that would not strongly discriminate against lines outside the nuclear core, since we are looking for evidence for ionizing radiation escaping into the surrounding gas. An aperture $0''.86$ in diameter was used to measure the lines; this is just over 3 times the FWHM of the diffraction limit at the wavelength of the [Ne VI] line. This aperture corresponds to a radius of ~400 pc (for all three), in agreement with the dimensions of winds in the galactic nuclei (E. González-Alfonso et al. 2017; I. Lamperti et al. 2022). We assumed the line profile to be a Gaussian with a FWHM of 500 km s^{-1} in all cases, again allowing for wind velocities seen in all three galaxies (E. González-Alfonso et al. 2017; I. Lamperti et al. 2022). The line location was masked, and the continuum was fit and subtracted with a 4th-degree polynomial. A Gaussian at the line location and velocity width of 500 km s^{-1} was fitted and integrated to find the line flux limits for the nondetected lines.

Around the wavelength of the [Ne VI] line, methane ice absorption is prominent (see Figure 1). We used models of the spectrum to allow accurate fitting (rather than just a polynomial fit to a continuum). The models for IRAS 14378-3651 and IRAS 23365+3604 were adequate using only methane ice, but for IRAS 17208-0014 the model combined methane and acetylene, generated along the lines similar to that described by V. Buiten et al. (2025) for Arp 220. The models are shown around the wavelength of the [Ne VI] line for comparison with the spectra in Figure 1. In addition, for the special case of the detected [Mg IV] line, the amplitude and

[5] Provided by David Law: https://github.com/STScI-MIRI/MRS-ExampleNB/tree/main/D2P_Notebooks: MRS_Flag_Badpix jupyter notebook.

[6] These pixels set by the various steps in the JWST pipeline had values of OTHER_BAD_PIXEL, NO_SAT_CHECK, and UNRELIABLE_FLAT. See https://jwst-pipeline.readthedocs.io/en/latest/jwst/references_general/references_general.html.

Table 2
High-excitation Line Strengths

Line	Wavelength (μm)	Ionization Potential (eV)	14378 Flux[a]	Error	17208 Flux[a]	Error	23365 Flux[a]	Error
S VIII	0.99157	281	0.64	0.52	0.31	0.56	−0.12	0.38
Cr VIII	1.0109	160	−0.16	0.47	−0.29	0.4	0.08	0.41
Fe XIII	1.0749	331	0.5	0.58	−0.59	0.41	0.47	0.63
Fe XIII	1.08	331	−0.41	0.37	0.55	0.96	−0.58	0.53
S IX	1.2523	329	−0.67	0.6	0.59	0.51	−0.71	0.43
Si X	1.43049	351	−0.03	0.83	0.28	0.73	−0.25	0.55
Ti VI	1.7156	99	−2.39	1.41	−1.44	0.76	2.05	1.14
S XI	1.9201	448	−1.83	1.11	0.73	0.29	−0.39	0.73
Si XI	1.932727	401	0.01	0.47	−0.19	0.5	0.08	0.81
Si VI	1.9646	167	0.54	0.47	−0.96	0.99	−0.08	0.36
Al IX	2.043	285	1.31	0.74	0.57	0.46	0.89	0.77
Sc V	2.3118	73	0.08	0.57	−1.45	2.47	1.61	0.6
Ca VIII	2.3211	127	−0.05	0.52	⋯	⋯	−0.28	0.48
Si VII	2.481	205	1.32	0.81	0.72	0.46	1.62	0.86
Si IX	2.585	303	0.84	0.59	0.36	0.35	0.22	0.94
Ar XI	2.59535	480	0.37	0.55	−0.34	0.45	−0.51	0.49
Al V	2.905	120	−0.18	0.32	0.04	0.35	0.36	0.42
Mg VIII	3.028	225	−0.13	0.24	0.18	0.29	−0.12	0.25
Ca IV	3.207	51	0.29	0.26	−0.04	0.17	0.47	0.21
Al VI	3.65971	154	−0.86	0.48	−0.19	0.26	−0.33	0.31
Al VIII	3.69	242	−0.16	0.36	0.53	0.29	−1.13	0.55
Si IX	3.929	303	0.07	0.33	⋯	⋯	0.08	0.31
Ca VII	4.0858	127	0.21	0.64	0.35	0.32	−0.47	0.45
Ca V	4.15937	67	−0.06	0.38	0.65	0.51	0.01	0.42
Ar VI	4.5292	80	0.18	0.47	0.68	1.02	1.17	0.79
Ne VI	7.6524	126	−1.15	1.2	0.78	2.1	−2.14	1.03
Fe VIII	7.815	99	0.55	1.04	1.58	2.45	−0.17	1.08
Cl IV	11.7619	40	0.47	0.32	−0.32	0.28	−0.2	0.42

Notes. 14378, 17208, and 23365 correspond to IRAS 14378-3651, IRAS 17208-0014, and IRAS 23365+3604, respectively.
[a] All fluxes are in units of 10^{-19} W m^{-2}.

width of the fitted Gaussian were left as free parameters when finding the flux, and the aperture size expanded to capture the full flux of the line.

For all lines, the error is found by selecting 30 spectral positions near to the line. For each position, we fitted a Gaussian with a width of 500 km s^{-1} to determine an amplitude for noise that could affect our line measurement. The noise was taken as the rms of the 30 fits. The line measurements are listed in Table 2. We quote the measured apparent strengths and the 1σ errors, rather than upper limits.

4. Results

4.1. Search for Traces of AGNs

4.1.1. The Near-infrared Spectrum

The near-infrared spectra of the three galaxies are shown in Figure 2. As seen from Table 2, none of the high-excitation lines potentially in these spectra were detected, with the exception of [Mg IV] (4.488 μm). Another potential hint of an AGN would be broad wings on the hydrogen recombination lines, particularly Brα where the extinction in minimized. However, as shown in Figure 3, none of the galaxies show any indication of this effect. The total line flux in IRAS 17208-0014 is dominated by a broad component that might be associated with outflows identified by D. S. N. Rupke & S. Veilleux (2013), S. Arribas et al. (2014), and S. García-Burillo et al. (2015), but the velocity structure of this galaxy is very complex (S. Baba et al. 2022). The FWHMs for the other two galaxies are ∼250 km s^{-1}.

4.1.2. Strength of the [Ne VI] Line

The [Ne VI] and [Ne V] lines both lie in spectral regions of relatively low interstellar absorption, which extend from 5 to 8 μm and from 13 to 16 μm (K. D. Gordon et al. 2021). This makes them ideal to search for heavily obscured AGNs. The upper limits on the high-excitation lines from this study are far below those obtained previously on the equivalent lines on the same galaxies with Spitzer/IRS. In C. E. Goldberg et al. (2024), we showed that the [Ne VI] 7.652 μm line is equivalent to the [Ne V] 14.32 μm line in strength and as a measure of AGN excitation; we have preferred the shorter-wavelength line because of its higher angular resolution. Neither line is detected in any of the four galaxies as shown in Table 3. The difference was limited to a factor of ∼10–20 for Arp 220 due to complexities in its molecular absorption spectrum, but the other three galaxies show significantly deeper limits relative to the previous Spitzer/IRS measurements.

C. E. Goldberg et al. (2024) showed that virtually all CT and nearly CT AGNs show a detectable level of emission in the [Ne V] line with Spitzer/IRS. This demonstrates that the obscuration viewed from the nuclei of these galaxies is CT in our direction, but has thinner spots where the ionizing flux can escape to excite this line in the surrounding gas. The presence of this escaping flux, indicated by these lines, allows us to detect a buried AGN indirectly. We term this process as "seeing around the corner." The Spitzer limits for these ULIRGs are sufficiently close to the detections for typical CT

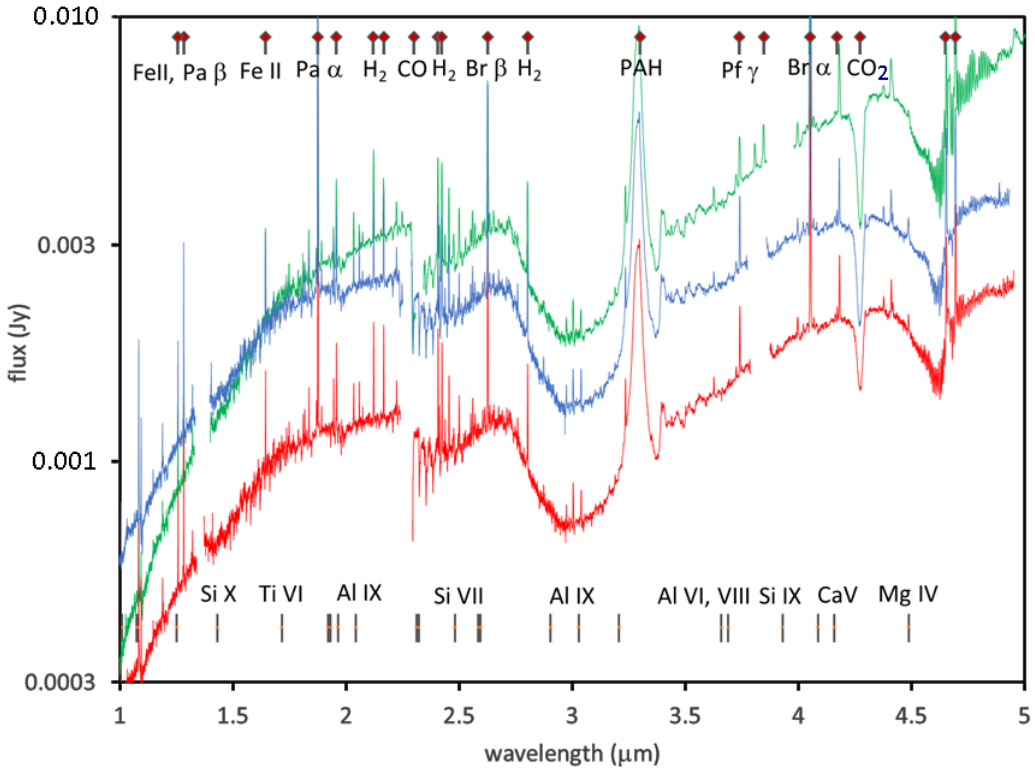

Figure 2. 1 to 5 μm spectra: (1) IRAS F17208-0014 (top, green), (2) IRAS 14378-3641 (middle, blue; reduced by a factor of 0.8), and (3) IRAS 23365+3601 (bottom, red; reduced by a factor of 0.5). The top diamond symbols indicate the wavelengths of a number of "standard" lines as well as the CO_2 absorption, while the lower vertical lines are the high-excitation lines we have searched for in this paper. Not all lines are labeled to minimize clutter; the missing high-excitation line identifications are provided in Table 2. All the spectra are at rest wavelengths.

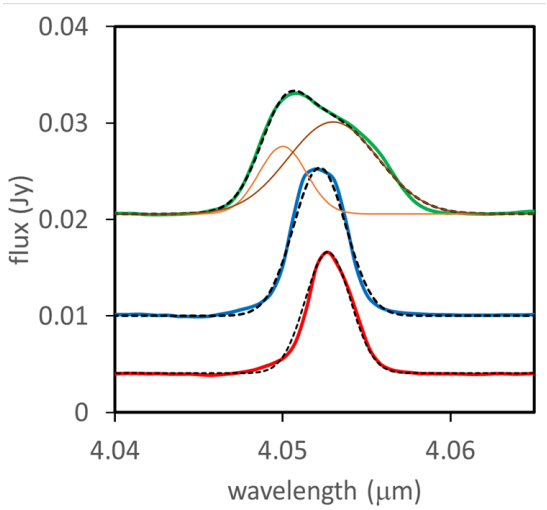

Figure 3. Spectra of Brα (rest frame): (1) IRAS F17208-0014 (top, green), (2) IRAS 14378-3641 (middle, blue), and (3) IRAS 23365+3601 (bottom, red). The spectra have been displaced vertically for clarity. The dashed lines are Gaussian line profiles fitted to the observed spectra. In the case of IRAS F17208-0014, two Gaussians were used, displaced by 220 km s^{-1}. The broader and longer-wavelength component has a FWHM of ~500 km s^{-1} and is displaced by ~70 km s^{-1} to the red and the FWHM of the shorter one is ~250 km s^{-1}, ~150 km s^{-1} to the blue. None of the lines show broad wings.

AGNs that they permitted the interpretation that all these objects are similar in this regard. However, the failure with JWST/MIRI to achieve detections 1 or 2 orders of magnitude fainter shows that these galaxies are not analogous to typical CT AGNs. Either the behavior of the nuclei in the galaxies in our sample is fundamentally different, or their AGNs are relatively weak. The latter hypothesis would be puzzling, given the well-studied conclusion that luminous AGNs should form in exactly this type of environment (late-stage mergers; e.g., P. F. Hopkins et al. 2008; G. F. Snyder et al. 2013; J. M. Gabor et al. 2016; C. Ricci et al. 2017; T. Kawaguchi et al. 2020; J. McKinney et al. 2021).

Table 3
Upper Limits (3σ) on [Ne v] (Spitzer) and [Ne VI] (JWST) Line Strengths

Galaxy	Spitzer/IRS[a] [Ne v]	JWST/MIRI [Ne VI]
IRAS 14378-3651	610	6.3
Arp 220[b]	1600	110
IRAS 17208-0014	480	17
IRAS 23365+3604	1130	3.9

Notes. All values are given in 10^{-20} W m^{-2}.
[a] From H. Inami et al. (2013).
[b] From C. E. Goldberg et al. (2024); the JWST/MIRI limit is compromised from the usual performance by strong molecular features.

5. Physical Properties of a Complete ULIRG Sample

To put our results in a broader context, we have assembled a complete sample of late-stage ULIRGs. The parent sample consists of all galaxies with $L(\mathrm{TIR}) \geqslant 10^{12}\,L_{\odot}$.[7] S. Stierwalt et al. (2013) used IRAC 3.6 μm images to classify the merger

[7] L(TIR) is the luminosity from 8 to 1000 μm from D. B. Sanders et al. (2003).

Table 4
Properties of the Complete Sample of Late-merger ULIRGs

Galaxy	$\log(M^*)$[a] ($M_\odot$)	Spect.[b]	CON?[c]	[Ne v][d] (10^{-17} W m^{-2})	$M_{BH}(M_\odot)$[e] Dynamics	$M_{BH}(M_\odot)$[f] Scaling	Ratio[g]	L_{AGN}[h] ($L_\odot$)	Edd.[i] Ratio
IRAS 05189-2524	10.93	Sy2	No	12.86	2.95×10^7 (1)	1.44×10^8	0.20	5.1×10^{11}	0.55
IRAS 07251-0248	10.93	H II	CON	<0.98	⋯	1.44×10^8	⋯	4.2×10^{11}	∼0.1
IRAS 08572+3915	10.49	LINER	CON	<1.07	8.4×10^7 (6)	2.82×10^7	3.4	7.6×10^{11}	0.28
IRAS 09022-3615	10.97	H II	No	<0.83	⋯	1.67×10^8	⋯	2.4×10^{11}	0.044
IRAS 10565+2448	10.99	H II	No	<0.89	⋯	1.80×10^8	⋯	3.1×10^{10}	0.005
IRAS 12112+0305	10.98	LINER	No	<0.70	4.60×10^7 (1)	1.74×10^8	0.27	3.8×10^{10}	0.026
IRAS 12540+5708	11.51	Sy1	Ne/12	<1.3	4.1×10^8 (4)	1.24×10^9	0.33	9.7×10^{11}	0.07
IRAS 13120-5453	11.33	Sy2	No	<1.26	⋯	6.36×10^8	⋯	3.6×10^{10}	0.002
IRAS 13428+5608	10.99	Sy2	⋯	10.02	1.04×10^9 (5)	1.80×10^8	5.55	2.1×10^{11}	∼0.006
IRAS 14348-1447	11.14	LINER	CON?	<0.21	1.13×10^8 (1)	3.14×10^8	0.36	8.0×10^{10}	0.022
IRAS 14378-3651	11.04	Sy2	No, Ne/12	<0.006	4.60×10^7 (2)	2.17×10^8	0.21	4.2×10^{10}	0.029
IRAS 15250+3609	10.8	LINER	⋯	<0.88	4.25×10^7 (1)	8.91×10^7	0.48	3.1×10^{11}	∼0.2
IRAS 15327+2340	10.97	LINER	CON, Ne/12	<0.11	1.40×10^8 (3)	1.67×10^8	0.84	1.1×10^{11}	0.025
IRAS 17208-0014	10.94	LINER	CON, Ne/12	<0.017	2.33×10^8 (1)	1.50×10^8	1.56	4.9×10^{10}	0.007
IRAS 19297-0406	11.28	H II	CON?	<0.52	⋯	5.28×10^8	⋯	7.0×10^{10}	0.004
IRAS 19542+1110	10.9	None	No	<2.10	⋯	1.29×10^8	⋯	5.5×10^{10}	0.013
IRAS 20551-4250	11.02	LINER	CON	<1.12	⋯	2.01×10^8	⋯	1.5×10^{11}	∼0.03
IRAS 22491-1808	10.92	H II	CON?	<0.68	5.60×10^7 (1)	1.39×10^8	0.40	1.3×10^{10}	0.007
IRAS 23365+3604	11.05	LINER	CON?, Ne/12	<0.004	3.71×10^7 (1)	2.25×10^8	0.17	5.4×10^{10}	0.045
Totals	⋯	⋯	⋯	⋯	4.26×10^9	⋯	⋯	4.15×10^{12}	0.030

Notes.
[a] From J. Shangguan et al. (2019).
[b] From E. Nardini et al. (2010), A. Efstathiou et al. (2022), and M. Pereira-Santaella et al. (2024).
[c] N. Falstad et al. (2021) and F. R. Donnan et al. (2023); IRAS 08572+3915 is added as a CON because of the extremely deep silicate absorption and lack of PAH or emission lines (e.g., S. Stierwalt et al. 2013). The designation "CON?" is for marginal cases or when the indicators are not conclusive. "Ne/12" indicates cases where the log of the ratio of the [Ne V] or [Ne VI] line strength to the 12 μm flux density is <4.3 (A. Alonso Herrero et al. 2024; this work), indicating a heavily embedded AGN (S. Yamada et al. 2024).
[d] From H. Inami et al. (2013), except for IRAS 12540+5708 (Mkn 231) from A. Alonso Herrero et al. (2024). For IRAS 14378-3651, IRAS 15327+2340 (Arp 220), IRAS 17208-0014, and IRAS 23365+3604, we show instead [Ne VI] from C. E. Goldberg et al. (2024) and this work; from the former reference, we expect the two neon lines to have the same flux.
[e] References: (1) = K. M. Dasyra et al. (2006); (2) = L. J. Tacconi et al. (2002); (3) = H. Engel et al. (2011); (4) = K. M. Leighly et al. (2014), R. I. Davies et al. (2004); (5) = U. Vivian et al. (2013); (6) = S. Onishi et al. (2024). When there are two black holes of comparable mass, we sum the masses. For Arp 220, the mass is for the W nucleus, but that of the E one is much smaller (C. E. Goldberg et al. 2024). The value for IRAS 12540+5708 (Mkn 231) is the average from the two works cited; the mass is difficult to measure accurately because the dynamics are dominated by a nearly face-on disk. For IRAS 17208-0014, we prefer the result based on stellar velocities in K. M. Dasyra et al. (2006) to the order of magnitude higher value based on the [Fe II] emission line from A. M. Medling et al. (2015) because the [Fe II] line is shock excited and likely to be highly turbulent, a prediction verified by the velocity image in A. M. Medling et al. (2015).
[f] Based on the "all, limits" relation in J. E. Greene et al. (2020), which is demonstrated to be preferred in Y. Sun et al. (2025).
[g] M_{BH} from dynamics divided by that from scaling.
[h] From total infrared luminosities in D. B. Sanders et al. (2003) and fractional AGN contributions from Table 6. Values below 10^{11} $L_\odot$ are unlikely to be accurate.
[i] Based on the M_{BH} from dynamics when it is available, otherwise on that from scaling.

stages if these galaxies; this band has the advantage of not being strongly affected by extinction. On this basis, we eliminated two (IRAS 09111-1002 and IRAS 23128-5919) that are classified as being in an earlier stage of evolution by S. Stierwalt et al. (2013). This yields the sample of 19 listed in Table 4, which indicates the four with JWST spectra in boldface. With the exception of IRAS 05189-2524 and IRAS 13428+5608, they all have upper limits on the [Ne v] 14.32 μm line that, while not as stringent as for the four in the JWST sample, strongly imply that virtually no emission by possible AGNs escapes into the larger galaxies. These limits could also, of course, indicate that some of them do not have luminous AGNs. In this section, we will interpret the measurements of the members of this sample (including the four measured with JWST) to derive basic properties: (1) covering fractions for the nuclei, (2) AGN luminosities, and (3) nuclear black hole masses. These properties will be interpreted further in the following section.

5.1. Covering Factors

5.1.1. JWST Sample

Arp 220, IRAS F17208-0014, and IRAS 23365+3604 contain CONs, and IRAS F14378-3651 is also heavily obscured (N. Falstad et al. 2021; F. R. Donnan et al. 2023). This classification is based on extremely high HCN-vib luminosities, which arise in regions of strong 14 μm radiation intensity. However, these observations leave open the possibility of lower-density sight lines providing escape paths for ionizing radiation that allow the "seeing around the corner" in typical CT AGNs. Such escaping radiation is required if the AGN is to have a strong far-infrared output, as a result of dust heated far from the AGN in its host galaxy (e.g., E. Roebuck et al. 2016; J. McKinney et al. 2021). The lack of high-excitation lines to the low levels we observe demonstrates that such paths are absent—it indicates that the high obscuration is

isotropic as viewed by any AGNs at the nuclei of these galaxies, i.e., the covering factor for AGNs by the thick circumnuclear material is essentially 100%. That is, the suggestions that estimates of the AGN luminosity need to include significant contributions to the far-infrared emission (E. Roebuck et al. 2016; M. Symeonidis et al. 2016; J. McKinney et al. 2021; M. Symeonidis 2022) are not applicable. We can treat the nuclei as calorimeters for the energy sources they contain. In general, determining covering factors is complex and inexact (M. Stalevski et al. 2016; C. Ricci et al. 2023), but these galaxies represent a point where these complexities are removed because their nuclei are completely covered.

5.1.2. Larger Sample

Of the 19 galaxies in the total sample, 11 have direct evidence for very dense interstellar material around their nuclei, either as CONs or through the ratio of the [Ne v] line to the 12 μm continuum (S. Yamada et al. 2024). Of the remaining eight, three are well-observed AGNs (IRAS 05189-2524, IRAS 13428+5608, and IRAS 15250+3608) and two appear to be purely H II galaxies (IRAS 09022-3615 and IRAS 10565+2448). Given the general evidence that the far-infrared in luminous infrared galaxies is not predominantly powered by AGNs (summarized in J. Lyu & G. Rieke 2022), we can assume that the estimates of the role of an AGN in the bolometric luminosities can be based on the mid-infrared properties. That is, similar to the four JWST-observed examples, we make the implicit assumption that any AGNs are sufficiently buried that their luminosity is captured by circumnuclear matter and emerges in the infrared, but there is no significant contribution to the far-infrared powered by energy escaping from the circumnuclear environment. The lack of any emission lines that would be excited by escaping nuclear energy strongly supports this implicit assumption.

5.2. AGN Luminosities

Starting with IRAS, it was apparent that AGNs have different mid- and far-infrared spectral energy distributions (SEDs) than star-forming galaxies, with no or weak PAH features and a stronger mid-infrared continuum. A number of studies have made use of this difference to separate the portion of infrared output associated with an AGN from the total infrared luminosity of a galaxy, which is typically dominated by far-infrared emission powered by young stars. These studies allow us to estimate the output of buried AGNs in ULIRGs (D. Farrah et al. 2003; E. Valiante et al. 2009; E. Nardini et al. 2010; T. Díaz-Santos et al. 2017; and others). We describe them below and summarize the results in Table 5.

1. The earliest example, D. Farrah et al. (2003), made use of AGN SED templates based on IRAS, ISO, and ground-based photometry. In three cases they attributed a large luminosity to a buried AGN through a large far-infrared flux, which would be contrary to the current understanding of AGN SEDs (J. Lyu & G. Rieke 2022). We have verified that modern star-forming SEDs (G. H. Rieke et al. 2009) fit the far-infrared in these cases. We therefore do not report the results in the table for IRAS 15250+3608, IRAS 22491-1808, and IRAS 23365+3604.
2. E. Valiante et al. (2009) decomposed Spitzer/IRS spectra between 5.5 and 6.85 μm using a star formation spectrum from M82 and a linear assumed AGN spectrum of arbitrary slope. To correct the 6 μm measurements of E. Valiante et al. (2009) to a ratio of AGN luminosity to bolometric luminosity, we used the formulation of E. Nardini et al. (2009) where 6 μm continuum measurements were available, and otherwise used a standard quasar continuum, adjusted to agree overall with the former approach.
3. As discussed in E. Nardini et al. (2009), the results of E. Nardini et al. (2010) are also based on Spitzer/IRS spectra using an average star-forming spectrum of a number of ULIRGs and an assumed AGN power law with a fixed slope of 1.5 (in frequency units) and fitting from 5 to 8 μm.
4. T. Díaz-Santos et al. (2017) estimated the AGN contribution to the mid-infrared from IRS spectra using a variety of emission features and the slope of the continuum between 15 and 30 μm. They then determined the AGN contribution to the infrared luminosity by applying bolometric corrections from S. Veilleux et al. (2009) that are based on averages over samples of ULIRGs and Palomar-Green quasars for star-forming and AGNs, respectively.

The various estimates are in reasonably good agreement given the range of analysis approaches. However, cases with significant AGN emission show scatter outside of the indicated errors, evidence for systematic differences among the four approaches. Averaging measurements dominated by systematic differences is not appropriate, so for all sources we assigned an adopted value. The scatter is not readily seen among the majority of sources with weak AGN signatures—all the approaches are able to agree when an AGN is not apparent.

The fractional luminosities for IRAS 14378-3651, IRAS 15327+2340 (Arp 220), IRAS 17208-0014, and IRAS 23365 +3604 in Table 5 are supported by additional measurements. As discussed in Section 2, X-ray data for all four indicate very low fractional luminosities. The case of Arp 220 is discussed in C. E. Goldberg et al. (2024): D. S. N. Rupke & S. Veilleux (2013) find that only 11% of the luminosity is possibly derived from an AGN; G. Risaliti et al. (2010) used L-band spectra to estimate that $2\% \pm 1\%$ of the bolometric luminosity comes from an AGN. For IRAS 17208-0014, J. Leja et al. (2018) use Prospector, including emission from dusty AGN torii, to fit the UV-IR broadband photometry, and conclude that $17^{+13}_{-6}\%$ of the 4–20 μm emission is powered by an AGN. Based on extensive modeling including high-angular-resolution 10 μm spectra, A. Alonso-Herrero et al. (2016) estimate that the AGN contributes 1% of the bolometric luminosity of the galaxy (they also estimate an AGN-powered fraction of ~31% at 5–15 μm through a $\sim 0\farcs5$ wide slit—they show that the nucleus is extended on this scale so this number is consistent with that from J. Leja et al. 2018).

5.3. Black Hole Masses

In this section, we show that estimates of the masses of the central supermassive black holes (SMBHs) in our sample from dynamics and by scaling from their stellar masses are in agreement. This will allow us to assign black hole masses to all 19 galaxies in the following discussion.

Table 5
Fractional AGN Luminosities

Galaxy	Log(L)[a] ($L_\odot$)	Farrah[b]	Valiante[c]	Nardini[d]	Diaz-Santos[e]	Adopted Ratio
IRAS 05189-2524	12.11	$0.32^{+0.06}_{-0.07}$	0.32 ± 0.02	$0.30^{+0.04}_{-0.08}$	0.60 ± 0.07	0.4
IRAS 07251-0248	12.32	⋯	0.06*	0.39 ± 0.04	0.14 ± 0.08	∼0.2
IRAS 08572+3915	12.1	$0.34^{+0.08}_{-0.02}$	$0.95^{+0.05}_{-0.18}$	$0.86^{+0.02}_{-0.03}$	0.47 ± 0.09	0.6
IRAS 09022-3615	12.26	⋯	0.16*	$0.09^{+0.01}_{-0.03}$	0.19 ± 0.06	0.13
IRAS 10565+2448	12.02	$0.05^{+0.02}_{-0.01}$	<0.05	<0.001	0.04 ± 0.01	0.03
IRAS 12112+0305	12.28	<0.001	<0.02*	<0.007	0.06 ± 0.03	0.02
IRAS 12540+5708	12.51	$0.30^{+0.07}_{-0.01}$	0.27 ± 0.02	0.34 ± 0.03	0.53 ± 0.12	0.3
IRAS 13120-5453	12.26	⋯	<0.04*	<0.012	0.04 ± 0.02	0.02
IRASF13428+5608	12.14	$0.11^{+0.02}_{-0.08}$	0.08 ± 0.03	$0.075^{+0.01}_{-0.02}$	0.31 ± 0.08	∼0.15
IRAS 14348-1447	12.3	$0.17^{+0.06}_{-0.08}$	0.03 ± 0.02	0.04 ± 0.01	0.09 ± 0.05	0.04
IRAS 14378-3651	12.15	<0.17	<0.02*	<0.013	0.05 ± 0.02	0.03
IRAS 15250+3609	12.02	N/A	0.12*	$0.51^{+0.04}_{-0.05}$	0.18 ± 0.16	∼0.3
IRAS 15327+2340	12.21	<0.006	0.04 ± 0.03	0.17 ± 0.02	0.09 ± 0.05	0.07
IRAS 17208-0014	12.39	<0.10	<0.05	<0.004	0.05 ± 0.03	0.02
IRAS 19297-0406	12.37	<0.12	<0.04*	<0.013	0.05 ± 0.03	0.03
IRAS 19542+1110	12.04	⋯	0.04*	0.04 ± 0.01	0.08 ± 0.02	0.05
IRAS 20551-4250	12.00	$0.30^{+0.02}_{-0.10}$	0.08*	0.26 ± 0.03	0.24 ± 0.05	∼0.15
IRAS 22491-1808	12.11	N/A	<0.08	<0.0007	0.02 ± 0.02	0.01
IRAS 23365+3604	12.13	N/A	0.02*	$0.07^{+0.03}_{-0.02}$	0.05 ± 0.02	0.04

Notes.
[a] Luminosity from 8 to 1000 μm.
[b] D. Farrah et al. (2003); the three cases with "N/A" had implausible AGN far-infrared SEDs.
[c] The f_{6AGN} fluxes were converted to fractional bolometric luminosity using Equation (5) in E. Nardini et al. (2009) and 6 μm fluxes from S. Veilleux et al. (2009), where those fluxes were reported (we assume 5% errors since errors are not reported). Otherwise, indicated by *, we determined a correction from the "normal" quasar SED (J. Lyu et al. 2017) and multiplied by 2 to put it on the same basis (see text). We do not report errors in these latter cases.
[d] E. Nardini et al. (2010).
[e] T. Díaz-Santos et al. (2017).

5.3.1. From Dynamics

All the black hole mass determinations from dynamics are summarized in Table 4. As explained in the footnotes to the table, the mass for IRAS F12540+5708 (Mkn 231) is difficult to measure accurately because the dynamics are dominated by a nearly face-on disk. For IRAS 17208-0014, we prefer the result based on stellar velocities in K. M. Dasyra et al. (2006) because the gas motions are likely to be dominated by turbulence.

5.3.2. From Scaling Relations

Whether ULIRGs as a class of galaxies have more or less massive black holes than predicted by scaling relations based on the host-galaxy stellar masses (i.e., the Magorrian relation) can be addressed from Table 4. We have averaged the logarithm of the ratios of dynamical SMBH masses to SMBH masses scaled from the stellar masses, so high and low values receive equal weight; the average is -0.22 ± 0.16 in the log, i.e., there is a slight but insignificant tendency for the dynamical values to be lower than the scaled ones. The rms scatter is 0.5 dex, similar to but slightly smaller than the overall scatter in the scaling relation of ∼0.8 dex (Y. Sun et al. 2025).

A. M. Medling et al. (2015) argued that the black holes in ULIRGs are overmassive compared with the Magorrian relation. This is not as drastic a disagreement with our conclusion as it seems, since the majority of the members of the eight-member sample in A. M. Medling et al. (2015) actually agree with scaling relations. Another perspective is supplied by S. Veilleux et al. (2009), who argue that the dynamical masses are systematically smaller than those from scaling. We prefer to conclude that they agree within the expected scatter with the scaling relation of J. E. Greene et al. (2020), which has been shown by Y. Sun et al. (2025) to be preferred compared with others available. The overall behavior is consistent with the suggestion by L. Colina et al. (2001) that most ULIRGs represent the merger of two sub-L_* galaxies.

This result contradicts the suggestion that black holes can grow substantially within ULIRGs before reaching a late merger stage. Substantial mass growth over the relevant interval is unlikely according to the E. E. Salpeter (1964) growth timescale, which shows that doubling the mass of a black hole under standard conditions takes tens of millions of years. This is consistent with simulations that show that black hole growth is modest during mergers (S. McAlpine et al. 2020). A. M. Medling et al. (2015) do identify galaxies where the black holes appear to be overmassive: IRAS 01364-1042 and NGC 2623. However, it is likely that they were already overmassive prior to their mergers and that this condition has persisted (P. H. Johansson et al. 2009).

6. Eddington Ratios

In this section, we will estimate the Eddington ratios for the full sample of 19 ULIRGs. If there are AGNs in these galaxies, in virtually every case they are sufficiently deeply embedded that their luminosities are thermalized and emerge in the infrared. We described the estimation of the AGN luminosities (or of upper limits to them) in Section 5.2. Section 5.3 describes the mass determinations. We take the SMBH masses

from dynamics when they are available, otherwise from scaling. The resulting values for the Eddington ratios can be found in the last column of Table 4.

Only 4/19 of the galaxies have estimated Eddington ratios $\geqslant$0.1. Of the cases with very low Eddington ratios, IRAS 09022-3615 and IRAS 10565+2448 have H II spectra and may not actually have AGN-based nuclei. With the exception of IRAS 13120-5453 and IRAS 19542+1110, the remainder have direct evidence for very strong nuclear obscuration. That is, there does not appear to be a significant amount of luminosity missing from our estimates that might result in an underestimate of the Eddington ratios.

The situation invokes the result from C. Ricci et al. (2023), who found that AGN covering factors increase with decreasing Eddington ratios. Their sample never reaches covering factors of near unity, as would be the case for our sample. However, their study was confined to relatively "conventional" AGNs, i.e., on a hard-X-ray-detected sample; only IRAS 05189-2524 and IRAS 13428+5608 = Mkn 273 among our galaxies have significant hard X-ray emission, and so the surrounding material for the rest may be significantly denser than for the Ricci sample. Thus, it is not surprising that our galaxies carry the trend C. Ricci et al. (2023) found to an extreme.

A broad variety of theoretical studies have predicted that late-stage mergers in ULIRGs should be characterized by very high rates of accretion onto the central black holes with resulting high Eddington ratios (P. F. Hopkins et al. 2008; G. F. Snyder et al. 2013; J. M. Gabor et al. 2016; C. Ricci et al. 2017; T. Kawaguchi et al. 2020; J. McKinney et al. 2021). These predictions in their simplest form are inconsistent with our results. It is possible that the high rates of accretion are intermittent, in which case the time-averaged behavior of our sample is of interest. A measure of that is given by the "totals" row of Table 4, where we show the sum of all the black hole masses and all the AGN luminosities, and find that the resulting Eddington ratio is 0.030. That is, as a whole these ULIRGs are emitting at low Eddington ratios and it is not likely that we have just observed them at an unlucky time. It is more likely that only a modest fraction of the late-stage ULIRGs behave as predicted by the models.

7. Conclusion

This paper completes the description of a program to detect emission lines indicative of high excitation, e.g., an AGN, in four late-stage merger ULIRGs. In none of these examples do we detect any indication of an AGN through these indicators. We conclude that any AGN, if indeed one exists, is so buried in an isotropic surrounding cloud that virtually none of its luminosity can escape. This validates luminosity estimates based on mid-infrared spectral behavior. On this basis, all four ULIRGs have AGNs that are accreting at no more than 0.1 of the Eddington rate.

We extend this study to a complete sample of 19 ULIRGs from the IRAS Bright Galaxy Sample. Only four of them have Eddington ratios $\geqslant$0.1. The Eddington ratios for the remaining 15 are well under 0.1. This result is contrary to the simple expectation from theoretical models which predict that the late-stage merger should be marked by very high rates of accretion onto the central black holes of the merging galaxies, with the impending emergence of a quasar. It appears that these high rates of accretion must be intermittent, or not to apply to all late-stage merger ULIRGs.

Acknowledgments

We thank Anne Medling and Vivian U for helpful comments. We also thank the referee for a very helpful report. Work on this paper was supported in part by grant No. 80NSSC18K0555, from NASA Goddard Space Flight Center to the University of Arizona. A.A.H. acknowledges support from grant No. PID2021-124665NB-I00, funded by MCIN/AEI/10.13039/501100011033 and by the ERDF, "A way to make Europe."

Facilities: JWST.

Software: NumPy (C. R. Harris et al. 2020), Astropy (Astropy Collaboration et al. 2022), Matplotlib (J. D. Hunter 2007).

Appendix
[Mg IV] Detections

[Mg IV] is the only high-excitation emission line detected in any of the galaxies, and it is found in all three as shown in Figure 4. Table 6 gives the total line strengths and the furthest extent from the nucleus that the line is detected. M. Pereira-Santaella et al. (2024) show that this line is prominent in the nucleus and outflow region in the Seyfert galaxy NGC 7469, but that it is also excited over extended areas due to shocks associated with supernovae and hence with star formation. We show below that the supernova excitation is most likely the case for our three galaxies and that the line does not indicate the existence of an AGN.

A.1. [Mg IV] versus Hu-12

To explore how [Mg IV] is excited, we take advantage of the NIRSpec IFU and map it in each galaxy. The Hu-12 (4.376 μm) hydrogen recombination emission line is a standard tracer of star formation. It is very close in wavelength to [Mg IV] (see Figure 4) so their relative strengths are not affected by extinction. We compare these two lines to determine how effectively the [Mg IV] traces star-forming regions.

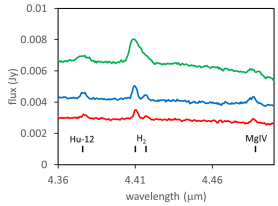

Figure 4. Spectra including Hu-12 and [Mg IV], for (1) IRAS F17208-0014 (top, green), (2) IRAS 14378-3641 (middle, blue), and (3) IRAS 23365+3601 (bottom, red). The spectrum of IRAS 23365+3601 has been multiplied by 0.7 for display purposes.

Table 6
[Mg IV] Detections in the Sample Galaxies, Along with the Outer Radius to Which Each Line is Detected

Galaxy	Line Strength (10^{-19} W m^{-2})	Detection Radius (pc)
IRAS 14378-3651	4.04 ± 0.66	558
IRAS 17208-0014	8.05 ± 0.75	1135
IRAS 23365+3604	1.55 ± 0.40	592

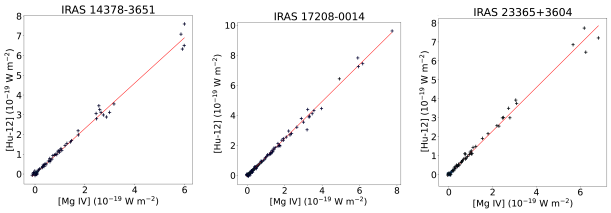

Figure 5. Plot of the Hu-12 and [Mg IV] flux measured from each spaxel in the NIRSpec IFU.

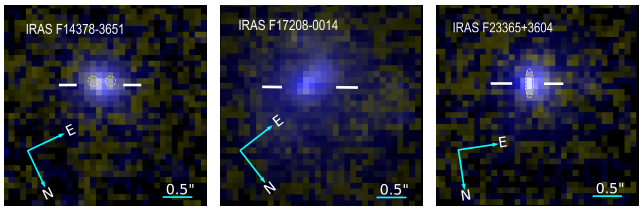

Figure 6. Stretched, color-enhanced images of the three sample galaxies with nuclear positions marked by two horizontal lines (14 40 59.0129 −37 04 31.855; 17 23 21.9510 −00 17 00.740; 23 39 01.2917 +36 21 08.412 (2000), respectively). Yellow represents [Mg IV] emission, and blue represents Hu-12 emission. Each image is 3″4 on a side. Where the [Mg IV] distribution differs significantly from that of Hu-12, we enclose the difference with a dashed line.

Table 7
Slope and *y* Intercept of the Increase in Hu-12 to Increase in [Mg IV] in Each IRAS Galaxy, as Shown in Figure 5

Galaxy	Slope	Intercept
IRAS 14378-3651	1.152 ± 0.003	−0.0004 ± 0.0317
IRAS 17208-0014	1.233 ± 0.006	−0.0102 ± 0.1377
IRAS 23365+3604	1.150 ± 0.004	0.0020 ± 0.0394

For each spaxel in the IFU, the luminosity of each line is measured across five wavelength planes to include the full luminosity of the lines. Then, the [Mg IV] and Hu-12 fluxes are plotted against each other, as shown in Figure 5. The line strengths are remarkably proportional to each other, resulting in a slope of nearly 1 and a *y* intercept of nearly zero for each galaxy. Table 7 shows the fit parameters. This behavior indicates that the [Mg IV] and Hu-12 lines have nearly identical luminosities and brighten at the same rate in regions of increasing star formation, similar to the results for other star-forming galaxies reported by M. Pereira-Santaella et al. (2024). We conclude that the [Mg IV] line is not excited by AGNs in any of our three galaxies.

A.2. Detailed Comparison of the Two Lines

To better understand the distribution of [Mg IV] and Hu-12, the lines are used to create color images in Figure 6. In each image [Mg IV] is mapped to yellow and Hu-12 is mapped to blue. The contrast of each image is increased by multiplying the colors in each channel by an exponent.

While the actual color differences are subtle, enhancing the images by increasing the saturation yields interesting insights into the nature of each galaxy. For IRAS 14378-3651, the Hu-12 line appears to mostly dominate the northern (bottom right in the image) region of the galaxy, while the [Mg IV] line is stronger in the core and southern (upper) regions. This indicates that the gas in the core and southern regions of the galaxy is more shocked, presumably from a high rate of supernovae, and may contain the strongest regions of current star formation in the galaxy. In IRAS 17208-0014, the Hu-12 line is stronger than the [Mg IV] throughout the entire galaxy, but is slightly weaker in the core. This may mean that there is less extreme star formation taking place in this galaxy compared to the others. Finally, Hu-12 is most prominent in the outskirts of IRAS 23365+3604 while the [Mg IV] is clearly stronger in the core. Thus, extreme star formation is likely taking place in the core of the galaxy.

ORCID iDs

George H. Rieke https://orcid.org/0000-0003-2303-6519
Victorine A. Buiten https://orcid.org/0009-0003-4835-2435
Charles E. Goldberg https://orcid.org/0000-0002-4901-7693
Jane Morrison https://orcid.org/0000-0002-9288-9235
Paul van der Werf https://orcid.org/0000-0001-5434-5942
Almudena Alonso-Herrero https://orcid.org/0000-0001-6794-2519
Stacey Alberts https://orcid.org/0000-0002-8909-8782
Nina Bonaventura https://orcid.org/0000-0001-8470-7094
Zhiyuan Ji https://orcid.org/0000-0001-7673-2257
Jianwei Lyu https://orcid.org/0000-0002-6221-1829
P. Rinaldi https://orcid.org/0000-0002-5104-8245
Meredith A. Stone https://orcid.org/0000-0002-9720-3255
Yang Sun https://orcid.org/0000-0001-6561-9443
Yongda Zhu https://orcid.org/0000-0003-3307-7525

References

Alonso Herrero, A., Hermosa Muñoz, L., Labiano, A., et al. 2024, A&A, 690, A95
Alonso-Herrero, A., Poulton, R., Roche, P. F., et al. 2016, MNRAS, 463, 2405
Arribas, S., & Colina, L. 2003, ApJ, 591, 791
Arribas, S., Colina, L., Bellocchi, E., et al. 2014, A&A, 568, A14
Astropy Collaboration, Price-Whelan, A. M., Lim, P. L., et al. 2022, ApJ, 935, 167
Auge, C., Sanders, D., Treister, E., et al. 2023, ApJ, 957, 19
Baba, S., Imanishi, M., Izumi, T., et al. 2022, ApJ, 928, 184
Buiten, V., van der Werf, P., Viti, S., et al. 2025, arXiv:2502.10271
Chandar, R., Caputo, M., Linden, S., et al. 2023, ApJ, 943, 142
Colina, L., Borne, K., Bushouse, H., et al. 2001, ApJ, 943, 142
Dasyra, K. M., Tacconi, L. J., Davies, R. I., et al. 2006, ApJ, 651, 835
Davies, R. I., Tacconi, L. J., & Genzel, R. 2004, ApJ, 613, 781
Díaz-Santos, T., Armus, L., Charmandaris, V., et al. 2017, ApJ, 846, 32
Donnan, F. R., Rigopoulou, D., García-Bernete, I., et al. 2023, A&A, 669, A87
Duc, P.-A., Mirabel, I. F., & Maza, J. 1997, A&AS, 124, 533
Duras, F., Bongiorno, A., Ricci, F., et al. 2020, A&A, 636, A73
Efstathiou, A., Farrah, D., Afonso, J., et al. 2022, MNRAS, 512, 5183
Engel, H., Davies, R. I., Genzel, R., et al. 2011, ApJ, 729, 58
Falstad, N., Aalto, S., König, S., et al. 2021, A&A, 649, A105
Farrah, D., Afonso, J., Efstathiou, A., et al. 2003, MNRAS, 343, 585
Gabor, J. M., Capelo, P. R., Volonteri, M., et al. 2016, A&A, 592, A62
García-Burillo, S., Combes, F., Usero, A., et al. 2015, A&A, 580, A35
Goldberg, C. E., Buiten, V. A., Rieke, G. H., et al. 2024, ApJ, 977, 55
González-Alfonso, E., Fischer, J., Spoon, H. W. W., et al. 2017, ApJ, 836, 11
González-Martín, O., Masegosa, J., Márquez, I., et al. 2009, ApJ, 704, 1570
Gordon, K. D., Misselt, K. A., Bouwman, J., et al. 2021, ApJ, 916, 33
Gowardhan, A., Spoon, H., Riechers, D. A., et al. 2018, ApJ, 859, 35
Greene, J. E., Strader, J., & Ho, L. C. 2020, ARA&A, 58, 257
Haan, S., Surace, J. A., Armus, L., et al. 2011, AJ, 141, 100
Harris, C. R., Millman, K. J., van der Walt, S. J., et al. 2020, Natur, 585, 357
Hopkins, P. F., Cox, T. J., Kereš, D., et al. 2008, ApJS, 175, 390
Hunter, J. D. 2007, CSE, 9, 90
Inami, H., Armus, L., Charmandaris, V., et al. 2013, ApJ, 777, 156
Iwasawa, K., Sanders, D. B., Evans, A. S., et al. 2009, ApJL, 695, L103
Johansson, P. H., Burkert, A., & Naab, T. 2009, ApJL, 707, L184
Kawaguchi, T., Yutani, N., & Wada, K. 2020, ApJ, 890, 125
Lamperti, I., Pereira-Santaella, M., Perna, M., et al. 2022, A&A, 668, A45
Leighly, K. M., Terndrup, D. M., Baron, E., et al. 2014, ApJ, 788, 123
Leja, J., Johnson, B. D., Conroy, C., et al. 2018, ApJ, 854, 62

Lyu, J., & Rieke, G. 2022, Univ, 8, 304
Lyu, J., Rieke, G. H., & Shi, Y. 2017, ApJ, 835, 257
McAlpine, S., Harrison, C. M., Rosario, D. J., et al. 2020, MNRAS, 494, 5713
McKinney, J., Hayward, C. C., Rosenthal, L. J., et al. 2021, ApJ, 921, 55
Medling, A. M., Vivian, U., Max, C. E., et al. 2015, ApJ, 803, 61
Nardini, E., Risaliti, G., Salvati, M., et al. 2009, MNRAS, 399, 1373
Nardini, E., Risaliti, G., Watabe, Y., et al. 2010, MNRAS, 405, 2505
Onishi, S., Nakagawa, T., Baba, S., et al. 2024, ApJ, 976, 106
Pereira-Santaella, M., García-Bernete, I., González-Alfonso, E., et al. 2024, A&A, 685, L13
Perna, M., Arribas, S., Lamperti, I., et al. 2024, A&A, 690, A171
Ricci, C., Bauer, F. E., Treister, E., et al. 2017, MNRAS, 468, 1273
Ricci, C., Ichikawa, K., Stalevski, M., et al. 2023, ApJ, 959, 27
Ricci, C., Privon, G. C., Pfeifle, R. W., et al. 2021, MNRAS, 506, 5935
Rieke, G. H., Alonso-Herrero, A., Weiner, B. J., et al. 2009, ApJ, 692, 556
Risaliti, G., Imanishi, M., & Sani, E. 2010, MNRAS, 401, 197
Roebuck, E., Sajina, A., Hayward, C. C., et al. 2016, ApJ, 833, 60
Rupke, D. S. N., & Veilleux, S. 2013, ApJ, 768, 75
Salpeter, E. E. 1964, ApJ, 140, 796
Sanders, D. B., Mazzarella, J. M., Kim, D.-C., et al. 2003, AJ, 126, 1607
Sanders, D. B., & Mirabel, I. F. 1996, ARA&A, 34, 749
Sanders, D. B., Soifer, B. T., Elias, J. H., et al. 1988, ApJL, 328, L35
Shangguan, J., Ho, L. C., Li, R., et al. 2019, ApJ, 870, 104
Snyder, G. F., Hayward, C. C., Sajina, A., et al. 2013, ApJ, 768, 168
Stalevski, M., Ricci, C., Ueda, Y., et al. 2016, MNRAS, 458, 2288
Stierwalt, S., Armus, L., Charmandaris, V., et al. 2014, ApJ, 790, 124
Stierwalt, S., Armus, L., Surace, J. A., et al. 2013, ApJS, 206, 1
Sun, Y., Rieke, G. H., Lyu, J., et al. 2025, ApJ, 983, 165
Symeonidis, M. 2022, MNRAS, 509, 3209
Symeonidis, M., Giblin, B. M., Page, M. J., et al. 2016, MNRAS, 459, 257
Tacconi, L. J., Genzel, R., Lutz, D., et al. 2002, ApJ, 580, 73
Teng, S. H., Rigby, J. R., Stern, D., et al. 2015, ApJ, 814, 56
Vivian, U., Medling, A., Sanders, D., et al. 2013, ApJ, 775, 115
Valiante, E., Lutz, D., Sturm, E., et al. 2009, ApJ, 701, 1814
Veilleux, S., Rupke, D. S. N., Kim, D.-C., et al. 2009, ApJS, 182, 628
Yamada, S., Ueda, Y., Kawamuro, T., et al. 2024, ApJ, 965, 153
Zubovas, K., Bialopetravičius, J., & Kazlauskaitė, M. 2022, MNRAS, 515, 1705